THERMAL RADIATION FROM CRYOGENIC HYDROGEN JET FIRES

Cirrone, D.M.C., Makarov D. and Molkov V.
[1]Hydrogen Safety Engineering and Research Centre (HySAFER),
Ulster University, Shore Road, Newtownabbey, BT37 0QB, UK,
cirrone-dmc@email.ulster.ac.uk, dv.makarov@ulster.ac.uk, v.molkov@ulster.ac.uk

ABSTRACT

The thermal hazards from ignited under-expanded cryogenic releases are not yet fully understood and reliable predictive tools are missing. This study aims at validation of a CFD model to simulate flame length and radiative heat flux for cryogenic hydrogen jet fires. The simulation results are compared against the experimental data by Sandia National Laboratories on cryogenic hydrogen fires from storage with pressure up to 5 bar abs and temperature in the range 48-82 K. The release source is modelled using the Ulster's notional nozzle theory. The problem is considered as steady-state. Three turbulence models were applied and their performance compared. The realizable κ-ε model demonstrated the best performance in reproduction of experimental flame length and radiative heat flux. Therefore, it has been employed in the CFD model along with Eddy Dissipation Concept for combustion and Discrete Ordinates (DO) model for radiation. A parametric study has been conducted to assess the effect of selected numerical and physical parameters on the simulations capability to reproduce experimental data. DO model discretization is shown to strongly affect simulations, indicating 10x10 as minimum number of angular divisions to provide a convergence. The simulations have shown sensitivity to experimental parameters such as humidity and exhaust system volumetric flow rate, highlighting the importance of accurate and extended publication of experimental data to conduct precise numerical studies. The simulations correctly reproduced the radiative heat flux from cryogenic hydrogen jet fire at different locations.

1 INTRODUCTION

Cryo-compression is a competitive technique when storage of large quantities of hydrogen is needed [1]. Understanding of consequences of potential accidents with cryogenic release of hydrogen is fundamental to protect life and prevent property loss. Predictive models are needed for hydrogen safety engineering to calculate hazard distances in case of cryogenic unignited and ignited releases. Only few experiments have been performed to investigate thermal hazards from cryogenic jet fires. Friedrich et al.'s experiments performed in Germany concerned releases with pressures from 7 to 35 bar abs and temperature in the range 34-65 K [2]. Flame stability, combustion regimes and thermal radiation were analysed. Health and Safety Laboratory (HSL) in UK performed experiments on 60 l/min spills of LH_2 combustion and estimated that the minimum safety distance to avoid damage from jet fire thermal effects shall be about 14 m [3]. The most recent experiments on cryogenic hydrogen jet fires were conducted at Sandia National Laboratories (SNL) in USA [4]. The radiative thermal heat flux and flame length were analysed for release temperature 37-295 K and pressures up to 6 bar abs. It was found that for a constant mass flow rate, the radiative heat flux increases for colder release temperatures, as consequence of the higher flame residence time. The present study simulated a selection of these experiments using Fluent as computational engine. Several numerical studies investigated liquefied hydrogen (LH_2) unignited under-expanded jets [5]–[7], while there is a lack of investigations on ignited releases, i.e. jet fires. Therefore, the aim of this study is to develop and validate a CFD model to predict radiative heat fluxes from a cryogenic jet fire at different locations from the flame. As part of the model development, a parametric study has been conducted, giving insights into the effect of several parameters and model assumptions on simulation results.

2 VALIDATION EXPERIMENTS

The experiments were conducted at the Turbulent Combustion Laboratory of SNL in USA. The main aim of the experiments was to investigate the ignition and flame characteristics of cryogenic under-expanded jet fires. The analysed scenarios were concerned with hydrogen releases with temperature in

the range 37-295 K and pressure 2-6 bar abs. The release temperature and pressure were maintained constant during each test and monitored upstream the interchangeable orifice of diameter 0.75 mm or 1 mm or 1.25 mm. The hydrogen was released vertically upward in the laboratory equipped with an exhaust gases collection system. The facility geometry and dimensions are presented in Figure 1. The exhaust hood volumetric flow rate was varied from approximately 5100 to 7650 m^3/h, depending on the hydrogen mass flow rate. The incident thermal radiation was monitored at 5 sensors located along the jet flame and at 0.2 m from the jet axis. The exact location of each sensor is shown in Figure 1. The flame length was given as average of the visible and infrared (IR) cameras images. 5 tests out of the entire set of experiments performed by SNL have been selected for the CFD model development and validation. Table 1 shows the details of the experimental operating conditions of the selected tests. The orifice diameter for selected tests was 1.25 mm.

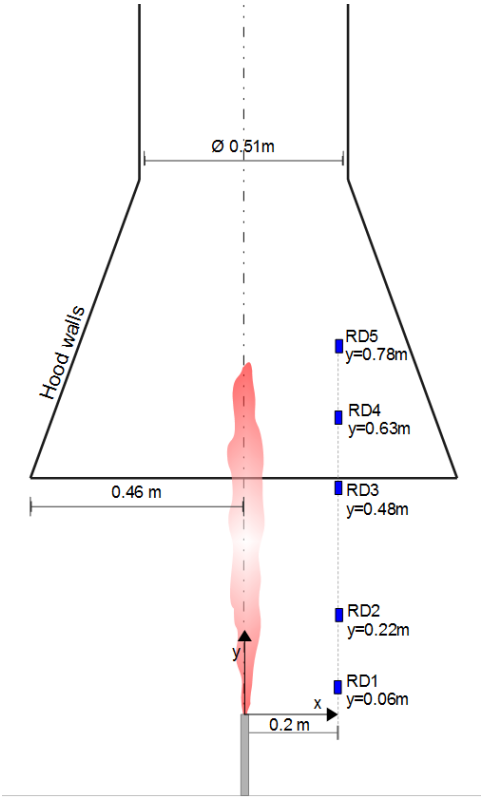

Figure 1. Scheme of the experimental set-up [8]

Table 1. Experimental operating conditions of 5 validation tests [8]

Test No.	Mass flow rate, g/s	Temperature, K	Pressure, bar abs
1	0.33	64	2
2	0.38	48	2
3	0.45	75	3
4	0.56	78	4
5	0.64	82	5

3 MODEL AND NUMERICAL DETAILS

3.1 Governing equations

The Reynolds-Averaged Navier-Stokes (RANS) conservation equations for mass, momentum, energy and species were solved:

$$\frac{\partial \rho}{\partial t}+\frac{\partial\left(\rho u_i\right)}{\partial x_i}=0\,, \tag{1}$$

$$\frac{\partial\left(\rho u_i\right)}{\partial t}+\frac{\partial\left(\rho u_i u_j\right)}{\partial x_i}=-\frac{\partial p}{\partial x_i}+\frac{\partial}{\partial x_i}\left(\mu+\mu_t\right)\left(\frac{\partial u_i}{\partial x_j}+\frac{\partial u_j}{\partial x_i}-\frac{2}{3}\frac{\partial u_k}{\partial x_k}\delta_{ij}\right)+\rho g_i\,, \tag{2}$$

$$\frac{\partial\left(\rho E\right)}{\partial t}+\frac{\partial}{\partial x_i}\left(u_i\left(\rho E+p\right)\right) \tag{3}$$

$$=\frac{\partial}{\partial x_i}\left[\left(k+\frac{\mu_t c_p}{Pr_t}\right)\frac{\partial T}{\partial x_i}-\sum_m h_m\left(-\left(\rho D_m+\frac{\mu_t}{Sc_t}\right)\frac{\partial Y_m}{\partial x_i}\right)+u_i\left(\mu+\mu_t\right)\left(\frac{\partial u_i}{\partial x_j}+\frac{\partial u_j}{\partial x_i}-\frac{2}{3}\frac{\partial u_k}{\partial x_k}\delta_{ij}\right)\right]+S_E\,,$$

$$\frac{\partial \rho Y_m}{\partial t}+\frac{\partial}{\partial x_i}\left(\rho u_i Y_m\right)=\frac{\partial}{\partial x_i}\left[\left(\rho D_m+\frac{\mu_t}{Sc_t}\right)\frac{\partial Y_m}{\partial x_i}\right]+S_m\,. \tag{4}$$

where ρ is the density, t is the time, i,j and k correspond to the Cartesian coordinates and u to the velocity components, p is the pressure, μ_t is the turbulent dynamic viscosity, δ_{ij} is the Kronecker symbol, g_i is the gravity acceleration, E is the total energy, c_p is the specific heat at constant pressure, Pr_t and Sc_t are the energy turbulent Prandtl and turbulent Schmidt numbers equal to 0.85 and 0.7 respectively, D_m is the molecular diffusivity of the species m, Y_m is the corresponding mass fraction, S_E and S_m are the source terms in the energy equation and m chemical specie transport equation.

Turbulence was accounted using the realizable κ-ε model [9], solving the transport equations for turbulence kinetic energy, κ, and turbulent dissipation rate, ε, as follow:

$$\frac{\partial\left(\rho k\right)}{\partial t}+\frac{\partial\left(\rho k u_i\right)}{\partial x_i}=\frac{\partial}{\partial x_i}\left[\left(\mu+\frac{\mu_t}{\sigma_k}\right)\frac{\partial k}{\partial x_i}\right]+G_k+G_b-\rho\varepsilon-Y_M\,, \tag{5}$$

$$\frac{\partial\left(\rho \varepsilon\right)}{\partial t}+\frac{\partial\left(\rho \varepsilon u_i\right)}{\partial x_i}=\frac{\partial}{\partial x_i}\left[\left(\mu+\frac{\mu_t}{\sigma_\varepsilon}\right)\frac{\partial \varepsilon}{\partial x_i}\right]+\rho C_1 S\varepsilon-\rho C_2\frac{\varepsilon^2}{k+\sqrt{\nu\varepsilon}}+C_{1\varepsilon}\frac{\varepsilon}{k}C_{3\varepsilon}G_b\,. \tag{6}$$

where G_k and G_b represent the generation of k by, respectively, mean velocity gradients and buoyancy, Y_M is the contribution of the fluctuating dilatation in compressible turbulence to the overall dissipation rate, σ_k and σ_ε are the turbulent Prandtl numbers for k and ε equal to 1 and 1.2, ν is the kinematic viscosity. C_1 is evaluated as function of the modulus of the mean rate of strain tensor, S. C_2 and $C_{1\varepsilon}$ are constants equal to 1.9 and 1.44, while $C_{3\varepsilon}$ is calculated as function of the flow velocity components with respect to the gravitational vector. Realizable κ-ε model performance was compared against standard κ-ε model [10] and RNG κ-ε model [11]. However, the specifics of these two models are not presented as they are not a part of the CFD model under validation.

Combustion was modelled through the Eddy Dissipation Concept (EDC) [12]. The rate of reaction of the species i is evaluated as follow:

$$R_i=\frac{\rho\left(\xi^*\right)^2}{\tau^*\left[1-\left(\xi^*\right)^3\right]}\left(Y_i^*-Y_i\right), \tag{7}$$

with $\xi^* = C_\xi \left(\frac{\nu\varepsilon}{\kappa^2} \right)^{1/4}$ and $\tau^* = C_\tau \left(\frac{\nu}{\varepsilon} \right)^{1/2}$

where Y_i is the species mass fraction, with value Y_i^* over the time scale τ^*, ξ^* is the fine scale length. C_ξ and C_τ are the volume fraction and times scale constants, equal to 2.1377 and 0.4082. The EDC model includes detailed chemical mechanisms. In the present model, 18 elementary reactions and 9 species are considered for hydrogen combustion in air. Complete description of chemical reaction mechanism is given in [13].

The DO model was employed to simulate radiation [14]. The Radiative Transfer Equation (RTE) is solved for a finite number of solid angles Ω' associated to the direction $\vec{s}$:

$$\nabla\left(I\left(\vec{r},\vec{s}\right)\vec{s}\right)+\left(\kappa+\sigma_s\right)I\left(\vec{r},\vec{s}\right)=\kappa n^2\frac{\sigma T^4}{\pi}+\frac{\sigma_s}{4\pi}\int_0^{4\pi}\mathrm{I}\left(\vec{r},\vec{s}^{'}\right)\Phi\left(\vec{s}\cdot\vec{s}^{'}\right)d\Omega^{'} \tag{8}$$

where the coefficient κ is the absorption coefficient, σ_s indicates the scattering coefficient and $\vec{r}$ is the position vector in $\vec{s}$ direction, n is the refractive index and Φ is the scattering phase function.

3.2 Modelling of release source

The operating pressure of the release in experimental tests is in the range 2-6 bar abs. At pressures above 2 bar abs an under-expanded jet is expected. The diameter of notional nozzle was calculated using Ulster's under-expanded jet theory [15], which assumes isentropic expansion, choked flow at the real nozzle, speed of sonic flow at the notional nozzle, and Abel-Noble equation of state (EOS) to describe the non-ideal behaviour of the gas. As the release is cryogenic, the problem must be handled carefully. The stagnation conditions are all located in the vapour/gas phase. During expansion, the saturation curve may be crossed leading to a multiphase release. However, even considering the worst-case scenario, i.e. lowest recorded temperature (48 K), highest pressure (6 bar) and isentropic expansion to ambient pressure, the resulting point will be in the gaseous phase. In the experiments, the lower temperatures (< 60K) are coupled to pressure equal to 2 bar, distancing the nozzle conditions from the saturation curve. The second consideration regards the validity of Abel-Noble EOS for cryogenic releases. Abel-Noble EOS was compared to NIST EOS [16], which is generally employed to model LH_2 releases [5]–[7]. Density comparisons for several pressures are shown in Figure 2. The deviation is negligible for the range of pressure under study (2-6 bar) while it becomes significant as the pressure increases. Thus, Abel-Noble EOS and the notional nozzle approach can be applied to the release cases under analysis.

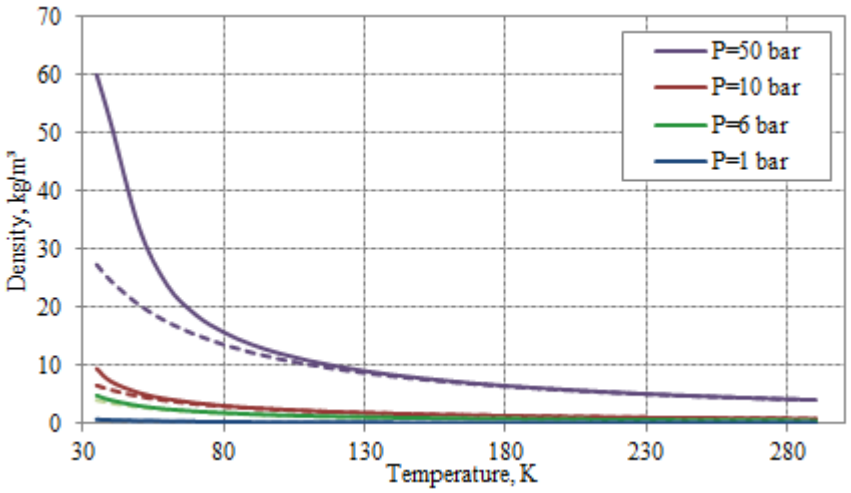

Figure 2. Effect of EOS on density evaluation: NIST (—) versus Abel Noble (--) equations

The calculated mass flow rate is compared against the experiments in Figure 3. The maximum deviation is about 10% and it is given for test 5. This discrepancy may be due to measurements uncertainty, as the measured mass flow rate is lower than a test with equal diameter and pressure but higher temperature (T=91 K, m=0.66 g/s), while colder temperature should correspond to increase of released mass. The evaluated notional nozzle conditions are presented in Table 2.

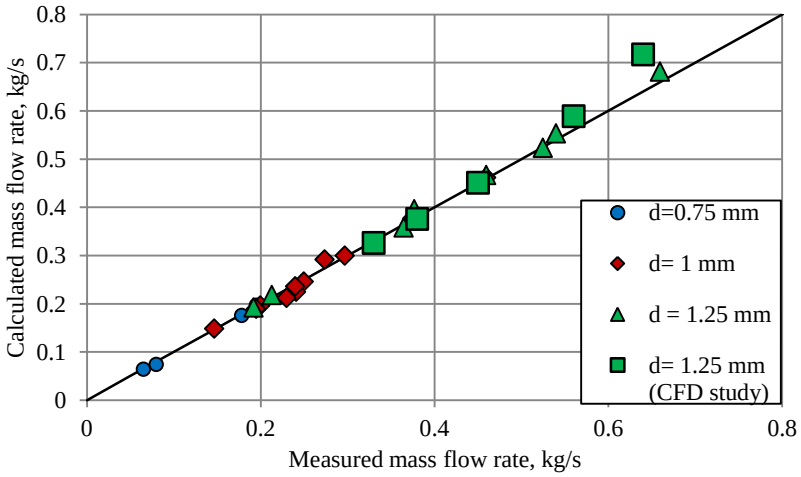

Figure 3. Calculated versus experimental mass flow rate

Table 2. Calculated notional nozzle conditions for the selected tests

Test No.	Inlet temperature, K	Inlet velocity, m/s	Density, kg/m^3	Notional diameter, mm	Calculated mass flow rate, g/s	Variation calculated mass flow rate from experiment, %
1	53	554.9	0.461	1.27	0.326	-1.26
2	40	480.6	0.614	1.27	0.376	-1.10
3	63	600.7	0.393	1.56	0.451	0.25
4	65	612.6	0.378	1.80	0.589	4.93
5	68	628.1	0.360	2.01	0.717	10.78

3.3 Computational domain and grid

Given the axisymmetric nature of the problem, a quarter of the domain was considered for the analysis. Two calculation domains were used to perform simulations:

- Rectangular domain with dimensions 0.5 m x 0.5 m x 3 m. The hood geometry was not included. The aim of the analysis was the investigation of the free jet fire characteristics without the effect of facility geometry and exhaust hood volumetric flow rate.

- Rectangular domain with dimensions 1.2 m x 1.2 m x 2 m. The hood geometry was included in the numerical grid.

The release source was approximated as square, with release area equal to the notional nozzle. As shown in Table 2, the 5 release tests resulted in 4 different notional nozzle diameters (D_{eff}). Thus, 4 numerical grids were created, adapting the release source and mesh to the test. The cell size varied from the notional nozzle size to about 10 cm in the far field. The maximum expansion ratio was 1.1 in the nozzle proximity. The number of control volumes (CVs) in the calculation domain varied, e.g. 267317 CVs in test 1, and 211587 CVs in test 2. The releases were treated as steady-state. The

velocity and temperature evaluated at the notional nozzle and indicated in Table 2 were imposed as inlet conditions at the nozzle. The turbulent intensity (TI) and turbulent length scale (TLS) were imposed as TI=25% and TLS=0.07D_{eff}, following the conclusions of the LES study on under-expanded hydrogen jet flame length and shape performed in [17]. TLS= 0.07D_{eff} is usually indicated for fully developed pipe flows [18]. The domain boundaries were modelled imposing a gauge pressure=0 and dry air was considered. However, section 4.1.4 analyses the case with moist air. The surface beneath the release pipe was modelled as non-slip adiabatic boundary. The radiometers, represented by 2x2 cm surfaces, were modelled as isothermal non-slip walls with emissivity 1. In this way, no radiation will be reflected by the surface and the received radiative heat flux will take account of the entire incident radiation. The only absorbing/emitting species in hydrogen combustion is water vapour. In this study, it was treated as a grey gas with Planck mean absorption coefficient defined as function of temperature and H_2O partial pressure. The function was determined from interpolation of Hubbard and Tien's data available in [19] and it will be indicated further in the text as HT. Scattering was not considered as it is negligible for combustion not involving soot. The Radiative Transfer Equation (RTE) was discretised using 5x5 angular divisions and 3x3 pixels, as suggested by [18]. The radiative discretisation will be varied in the range 5x5-15x15 angular divisions and 3x3-10x10 pixels in section 4.1.3. SIMPLE procedure was chosen for velocity-pressure coupling and convective terms were discretized using the second order upwind scheme. The stainless-steel hood walls considered in section 4.2 were modelled as non-slip walls with emissivity 0.6 [20]. The above described characteristics constitute the initial settings of the problem. Several parameters were varied in the proposed sensitive study and they will be indicated and discussed in the following sections.

4 RESULTS AND DISCUSSION

The aim of this section is to analyse the effect of the modifications of a set of parameters on the simulated thermal radiation. The sensitivity study is presented for test 1, with the exception of section 4.2.3, where the results are shown for tests 4 and 5. The effect of each variation was investigated singularly and in sequence, selecting each time the best value/sub-model and applying it in the following part of the study. The effect of numerical features, such as the turbulence model or radiation discretisation, was assessed for a free jet fire configuration and results are discussed in section 4.1. Analysis in section 4.2 includes the hood geometry, investigating the effect of the experimental settings, such as the exhaust gases extraction speed. Once the set-up of the model was completed, it was applied to the whole set of releases to validate it against experiments. Evaluations are shown in section 4.3.

4.1 Free jet fire

4.1.1 Effect of turbulence model

Simulations were performed for the standard κ-ε, RNG κ-ε and realizable κ-ε turbulence models. The resulting axial temperature distribution is reported in Figure 4, showing significant differences. Considering a 1300-1500 K region as corresponding to the visible flame length [21], the standard κ-ε, RNG κ-ε and realizable κ-ε models resulted in flame length included in the range, respectively, 0.5-0.59 m, 0.38-0.44 m and 0.63-0.72 m. Experimental flame length, evaluated as average of visible and infrared recordings, resulted 0.66 m. The realizable κ-ε turbulence model gives the best value compared to experiment. However, it must be highlighted that flame length evaluations in experiments and simulations are somehow arbitrary and uncertain, mining the reliability of results. The different temperature distribution affects strongly the radiative heat flux, shown in Figure 5, where the 5 diamonds of each curve represent the records at the 5 sensors. The realizable κ-ε model shows the best agreement with experiment.

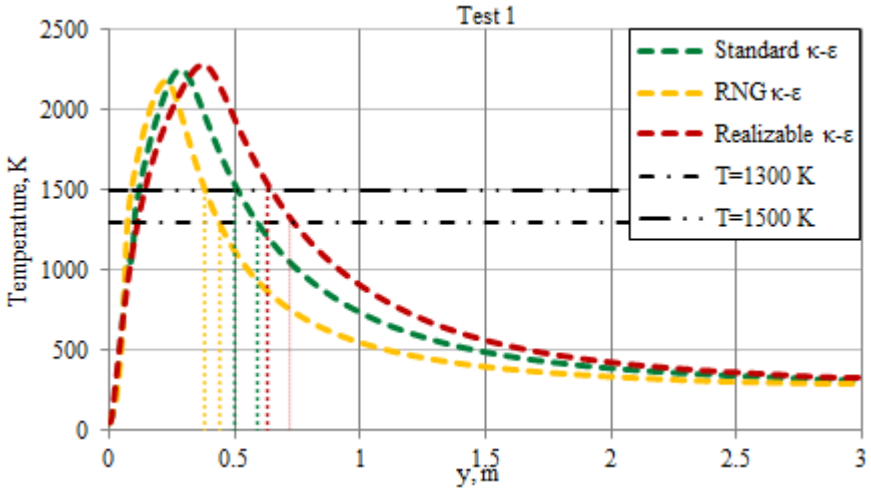

Figure 4. Effect of turbulence model on axial temperature distribution

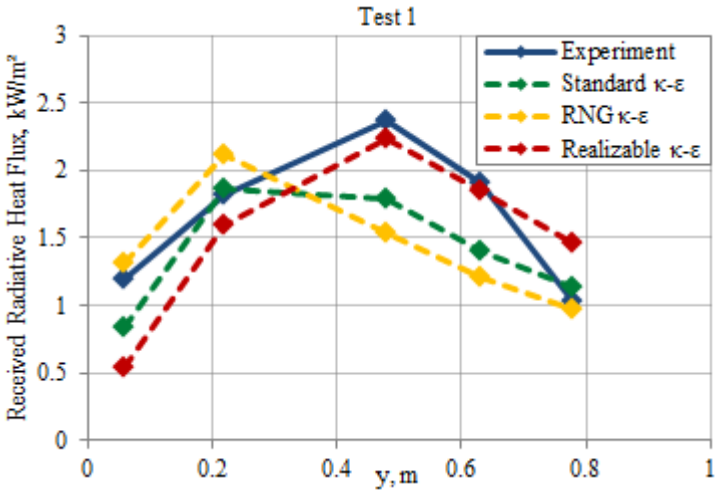

Turbulence model	*Standard κ-ε* *RNG κ-ε* *Realizable κ-ε*
TI and TLS	25%, 0.07D_{eff}
Angular divisions	5x5
Angular pixels	3 x 3
mf_{H2O}	0
Absorption coefficient	HT
Sc_t	0.7

Figure 5. Effect of turbulence model on radiative heat flux

4.1.2 Effect of inlet turbulence intensity and turbulence length scale

The current section is aimed to define the appropriate turbulence quantities at the inlet flow, i.e. at the notional nozzle exit. Indeed, these parameters affect the mixing occurring between the fuel and oxidizer, influencing the flame shape and species distribution in the jet fire. The flow perturbations at the inlet were modelled in terms of turbulence intensity and turbulence length scale. The case employing TI=25% and TLS=0.07·D_{eff} was compared to: a) TI=4% and TLS=0.07·D_{eff}, based on experimental observations on air under-expanded jets [22]; b) TI=30% and TLS=0.33·D_{eff}, based on the results of a parametric study conducted at HySAFER on hydrogen jet concentration decay. Figure 6 demonstrates that the turbulence inlet parameters affect the radiative heat flux only in proximity of the release point. However, the difference is negligible for turbulence intensity and turbulence length scale lower than, respectively, 30% and 0.33·D_{eff}. The effect on flame length was limited to ±2 cm variation. A further analysis was conducted for TI=30% and TLS=0.07·D_{eff}. The similarity of the results to the cases with equal TLS and different TI indicate that TLS is the cause of the variation for 30% and 0.33·D_{eff}. However, if for 30% and 0.33·D_{eff} case the prediction improves for radiation sensor 2, it worsens for sensor 1. Therefore, the selected inlet conditions are turbulence intensity 25% and turbulence length scale 0.07·D_{eff}.

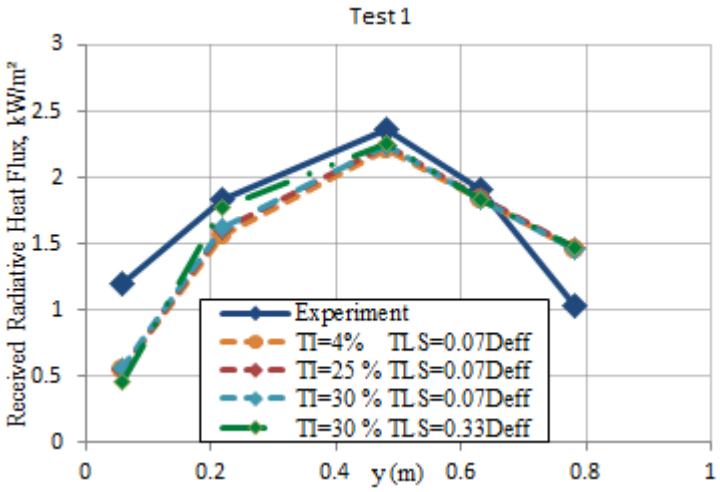

Turbulence model	Realizable κ-ε
TI and TLS	*4 %, 25%, 30% 0.07D eff, 0.33D eff*
Angular divisions	5x5
Angular pixels	3 x 3
mf_{H2O}	0
Absorption coefficient	HT
Sc_t	0.7

Figure 6. Effect of inlet turbulent intensity and turbulent length scale

4.1.3 Effect of radiation model angular discretisation

The number of Theta and Phi divisions determine the number of control angles associated to the RTE. 5x5 divisions are generally suggested for problems involving small geometry features and strong variation of temperature in space [18]. Under-prediction of radiative heat flux at the radiometers located in proximity of the release point may be due to insufficient angular discretisation, preventing the sensors to receive the radiation emitted by the flame along all its length. Thus, the number of divisions was increased, maintaining the same number of pixels. Comparisons for 5x5, 7x7, 10x10 and 12x12 are shown in Figure 7. Case with 15x15 was also analysed but not reported in Figure 7, as it practically overlaps the curves with 10x10 and 12x12 divisions. It was found that the angular discretisation has a great effect on the recorded radiative heat flux. Over 10x10 divisions the results are not sensitive to any further refinement. 10x10 was chosen as it is the adequate compromise between accuracy of the results and computational time (simulation time from 5x5 case increases by 1.9 for 10x10 and 2.4 for 12x12 angular divisions).

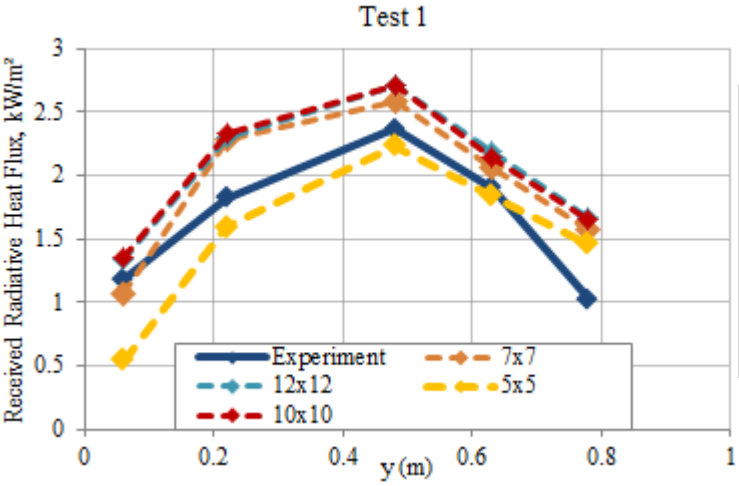

Turbulence model	Realizable κ-ε
TI and TLS	25%, 0.07Deff
Angular divisions	*5x5, 7x7, 10x10, 12x12, 15x15*
Angular pixels	*3x3, 10x10*
mf_{H2O}	0
Absorption coefficient	HT
Sc_t	0.7

Figure 7. Effect of number of angular divisions (3x3 pixels)

The Theta and Phi pixels take account of any control angle overhang. When the control volume face is not aligned to the global angular discretisation, control angles may be partially outgoing and partially incoming to the face. Pixelation subdivides each control angle in smaller portions where energy can be treated as incoming or outgoing. 3x3 pixels are usually suggested for problems involving symmetry [18]. The number of pixels was increased to 10x10 and no variation was sensed in the results. The

reason may be due to the use of a rectilinear hexahedral mesh, where the control volumes faces are aligned to the angular discretization, preventing the control angle overhang problem to arise. Thus, 3x3 pixels are sufficient to obtain reliable results and they were used with 10x10 angular divisions in the following analysis.

4.1.4 Effect of air humidity

The initial assumption of dry air for a controlled laboratory environment may not be adequate and the effect of water vapour presence must be assessed. The amount of water vapour in air is highly variable, depending on location and time. Mass fraction equal to 0.008 was assumed, according to the average meteorological data for SNL location, i.e. relative humidity equal to 74% and temperature 288 K [23]. As shown in Figure 8, the presence of water vapour has a significant effect on simulation results, remarking how indispensable is the availability of accurate description of various test conditions from experimentalists, including relative humidity. In the following sections, moist air will be considered, as it is more realistic and it provides better agreement with experiments.

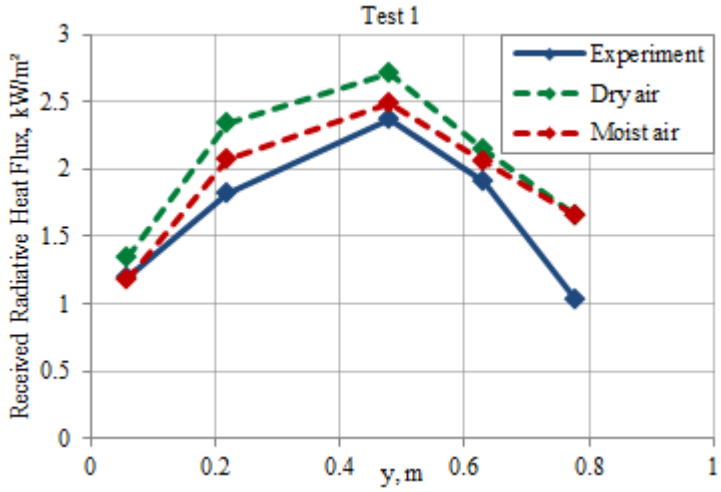

Turbulence model	Realizable κ-ε
TI and TLS	25%, 0.07D_{eff}
Angular divisions	10x10
Angular pixels	3x3
mf_{H2O}	*0, 0.008*
Absorption coefficient	HT
Sc_t	0.7

Figure 8. Effect of water vapour presence in air

4.1.5 Effect of absorption coefficient

Hubbard and Tien's Planck mean absorption coefficient (HT) was compared to the coefficient evaluated according to Yan et al.'s (Y) calculations [24]. The two coefficients mainly differ for temperatures lower than 800 K, where HT coefficient is higher than Y coefficient. As shown in Figure 9, this difference is translated in less radiation at the sensors located close to the release point, as radiation from the flame has a longer distance to cover and, because of higher absorption coefficient, greater chance to be absorbed. Given the better agreement with experiments, HT formulation was selected for the model.

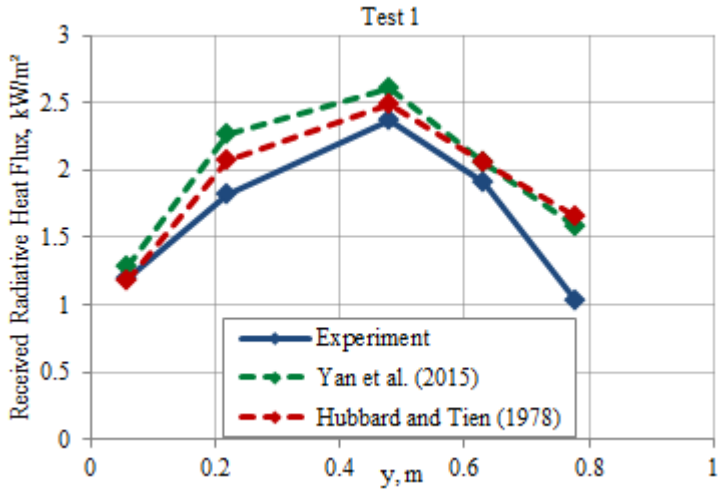

Turbulence model	Realizable κ-ε
TI and TLS	25%, 0.07D_{eff}
Angular divisions	10x10
Angular pixels	3x3
mf_{H2O}	0.008
Absorption coefficient	*HT, Y*
Sc_t	0.7

Figure 9. Effect of absorption coefficient

4.2 Hood inclusion in the geometry

The laboratory was equipped with an exhaust gases system. Therefore, the combustion can be affected by the flow imposed at the hood. The extension of the computational domain including the hood was decided according to a sensitivity study on the domain size. The width of the domain was changed from 0.7 m to 1.2 m. Maximum variation of radiative heat flux of about 8% was detected on sensor RD1, leading to the choice of domain size=1.2 m. To ensure that the domain boundaries are located sufficiently far from the area of interest, an additional sensitivity analysis was conducted on the domain boundary conditions. Turbulence kinetic energy and turbulent dissipation rate were varied from, respectively, $1.5 \cdot 10^{-4}$ m^2/s^2 and $3.0 \cdot 10^{-6}$ m^2 (evaluated for the analysis in section 4.2) to unitary values. The effect on radiative heat flux was confined to 4% variation, which was considered acceptable considering the needs to minimize the impact of boundary conditions on simulation results and to limit the required computational time. A complementary grid independency test is included in the authors' plans to assure full compliance with the CFD model evaluation protocol [25]. Figure 10 shows the comparison between the results of the free jet fire and the configuration including the hood. The removal of the combustion products by forced ventilation caused a decrease of radiative heat flux, reaching over 30% reduction. A further observation shall be made on emissivity for the stainless steel of the hood, as it may vary in a wide range according to the material composition and the maintenance status. A parallel analysis, not shown in Figure 10, on the variation of the hood surfaces emissivity was conducted, varying it from 0.60 to 0.07 [20]. The maximum increase was +8% and it was detected on sensor RD5. Emissivity of 0.60 will be used in the following simulations.

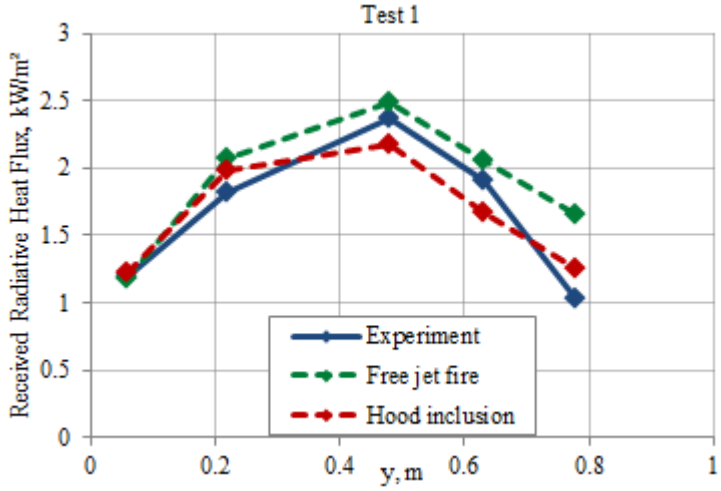

Turbulence model	Realizable κ-ε
TI and TLS	25%, 0.07D_{eff}
Angular divisions	10x10
Angular pixels	3x3
mf_{H2O}	0.008
Absorption coefficient	HT
Sc_t	0.7
V_{hood}	7 m/s

Figure 10. Effect of hood inclusion in the calculation domain (stainless steel emissivity=0.60)

4.2.1 Effect of turbulent Schmidt number

The turbulent Schmidt number, Sc_t, was changed in the range 0.7-1. The variation affected the temperature and species distribution in the jet. Figure 11 shows that the increase of Sc_t causes the radiative heat flux from the first portion of the flame to decrease, while it has the opposite effect for the second half. The reason is due to the flame highest temperature region movement towards the flame tip, thus increasing the emitted radiation from the final part of the flame. Sc_t=0.9 was selected for the following analysis, as it reproduced better the experimental radiative heat flux distribution trend, decreasing the gap between simulation and experiment for the sensors recording the highest radiative heat flux. In addition, Sc_t=0.9 gave the best reproduction for axisymmetric jets in the review proposed by [26].

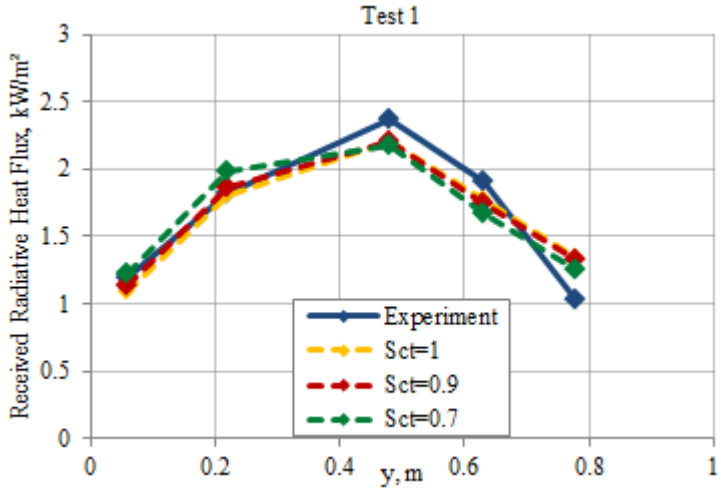

Turbulence model	Realizable κ-ε
TI and TLS	25%, 0.07D_{eff}
Angular divisions	10x10
Angular pixels	3x3
mf_{H2O}	0.008
Absorption coefficient	HT
Sc_t	*0.7, 0.9, 1*
V_{hood}	7 m/s

Figure 11. Effect of turbulent Schmidt number

4.2.2 Effect of extraction velocity in the hood

For each test, the volumetric flow rate of the ventilation system was adapted to the released mass flow rate of hydrogen. The only available experimental data is the range of variation of the volumetric flow rate, 5100-7650 m^3/h, corresponding to extraction velocity 7.0 m/s and 10.5 m/s respectively. No exact data for each test is available. Therefore, the minimum fumes speed has been considered in sections 4.2 and 4.2.1, based on the assumption that since the hydrogen mass flow rate (0.33 g/s) is closer to the minimum of the released mass range (about 0.1 g/s), the consequent extraction velocity will be more likely to be similar to the minimum of 7.0 m/s. However, tests 4 and 5 are characterised by a higher mass flow rate of 0.56-0.64 g/s, which is closer to the maximum mass flow rate of the overall tests set (0.7 g/s). Thus, fumes speed should be closer to 10.5 m/s rather than 7.0 m/s. This section aims to analyse the effect of the ventilation velocity on such releases, analysing the cases with minimum and maximum volumetric flow rate imposed at the hood as extreme cases. Figure 12 shows the effect of the hood extraction speed on the radiative heat flux. Since minimum and maximum limits were considered, the radiative heat flux curve simulating the actual fumes speed should be located between the green and red dashed curves, representing, respectively, the simulations for 7.0 and 10 m/s. For both the releases, considering the minimum extraction velocity led to a considerable overestimation (+36%) of the radiative heat flux for the sensors more exposed to the radiation from combustion products. The increase of the extraction velocity to the maximum limit, led to a reasonable reproduction of the experimental data, with deviations contained in the range ±14%. Therefore, extraction velocity of 10.5 m/s is considered for tests 4-5, while 7.0 m/s is considered for releases 1-3.

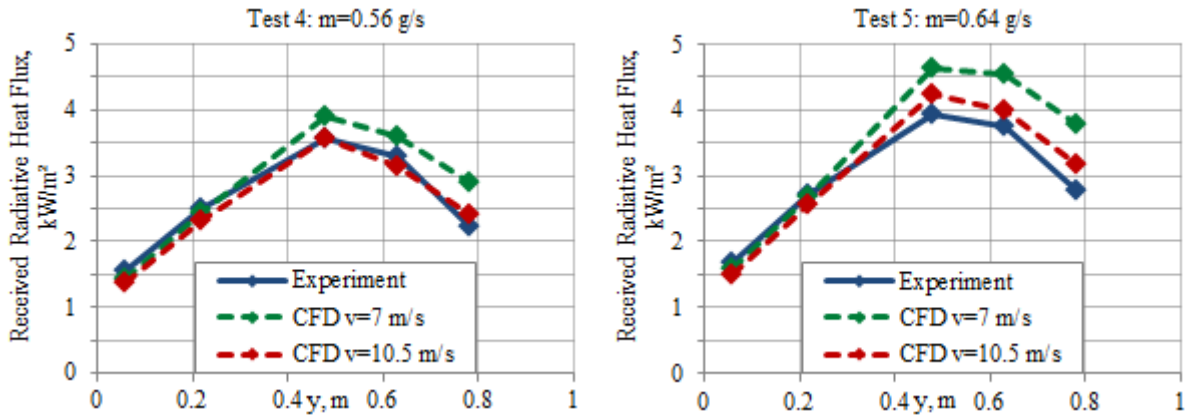

Figure 12. Effect of the hood extraction velocity in tests 4 and 5

4.3 Definition of model set-up based on the parametric study and validation

Following the conclusions of the previous sections, the best settings for the predictive model were identified and they are summarized in Table 3.

Table 3. Model set-up

Turbulence model	Realizable κ-ε
Turbulence intensity and length scale	25% and 0.07D
Angular divisions	10 x 10
Angular pixels	3 x 3
Water vapour mass fraction	0.008
Absorption coefficient	Hubbard and Tien (1978)
Turbulent Schmidt number	0.9
Velocity at the hood	Tests 1,2,3: v=7.0 m/s Tests 4,5: v=10.5 m/s

Results for the 5 tests are shown in Figure 13. Experimental radiative heat flux is predicted in simulations within ±15%, which is acceptable for safety engineering design accuracy. There is one exception, i.e. the overestimations of flux at 5th sensor for tests 1 and 2, where radiation is 29% and 17.5% higher respectively. It must be reminded that this sensor is the most affected by the hood characteristics taken in simulations, such as the material emissivity or the hood geometry, which is approximated as square. In addition, the 5th sensor is the most exposed to the water vapour of the jet flame, strongly affected by the velocity field imposed by the extraction system. Since no precise volumetric flow rate was available for each test, the assumption of either minimum or maximum flow velocity in the hood can lead to inaccuracy of results. The water vapour, while accumulating and cooling down, may also be affected by condensation, which is not taken in account in simulation. Experimental data on relative humidity were not available. Thus, the annual average for California (74%) was accepted. However, relative humidity is generally lower in environments where controlled air ventilation systems are present, such as combustion or chemical laboratories. Therefore, the slight under predicting trend present in most of the tests might be caused by such approximation.

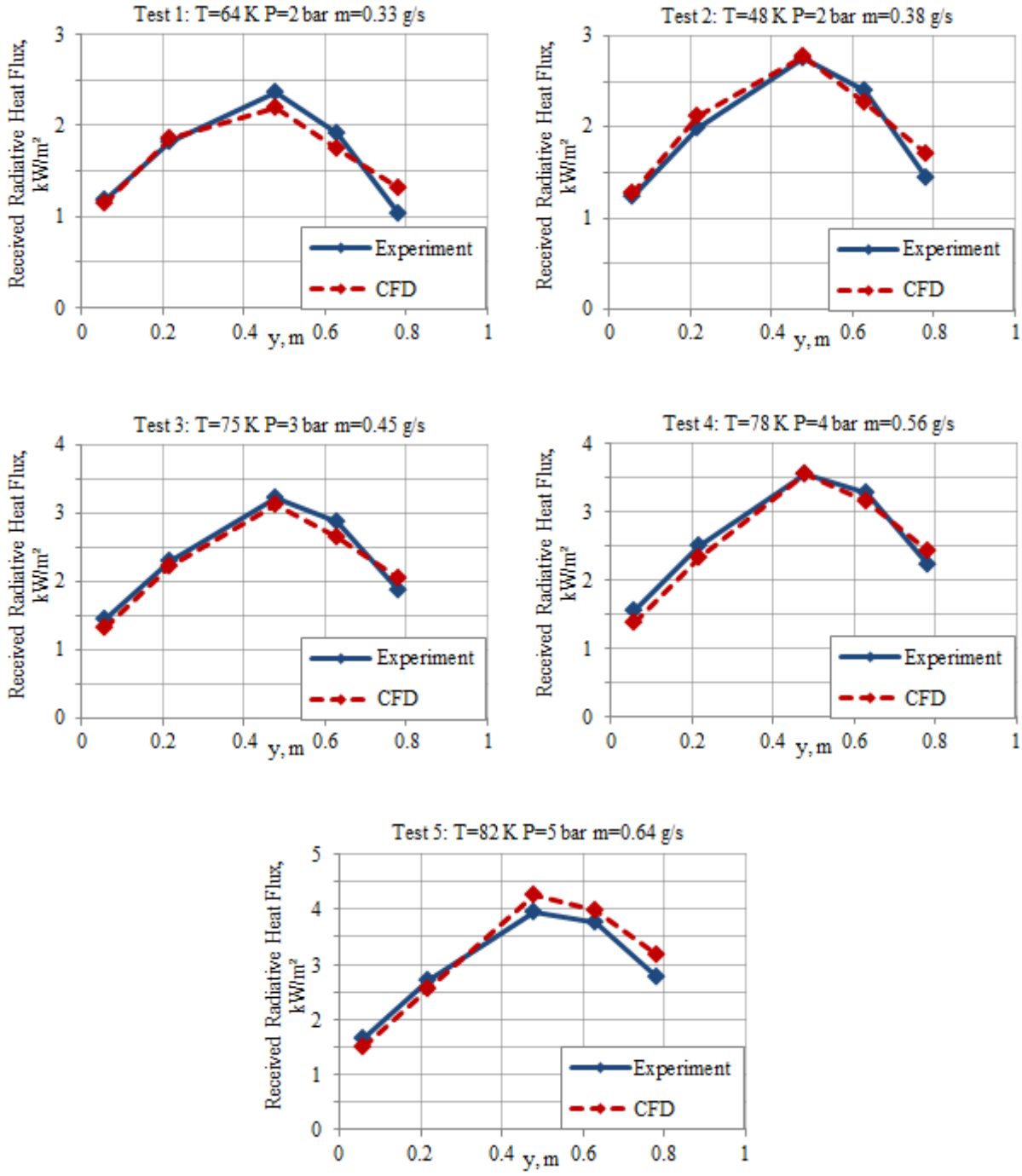

Figure 13. Radiative heat flux evaluation for validation experiments (model set-up: Table 3)

Table 4 reports the flame length evaluations based on the range of temperature 1300-1500 K and OH mole fraction=10^{-3}. In general, the simulated flame length resulted somewhat longer than reported by experimentalists. The difference becomes more significant for jet fires in tests 4 and 5. This can be due to the mass flow rate overestimations in simulations by, respectively, 5% and 10% of the release source modelling (Table 2). Similarly, overpredictions were expected for the radiative heat flux, mainly for test 5. However, the maximum deviation was 14%, maintaining an acceptable accuracy of the results.

Table 4. Experimental and calculated flame length

Test No.	**1**	**2**	**3**	**4**	**5**
Experiment, m	0.66	0.7	0.72	0.74	0.78
CFD 1300 K, m	0.74	0.80	0.85	0.94	1.02
CFD 1500 K, m	0.65	0.70	0.74	0.82	0.88
CFD $mf_{OH} = 0.001$, m	0.67	0.76	0.78	0.88	0.94

5 CONCLUSIONS

Simulations of cryogenic hydrogen jet fires were conducted to develop a predictive CFD model for assessment of thermal hazards. The simulations were validated against experiments in the range of pressures 2-5 bar abs and temperatures 48-82K. Release source was modelled using the notional nozzle theory [15]. Three turbulence models were compared and realizable κ-ε model demonstrated the best performance in reproducing the measured flame length and radiative heat flux. A sensitivity analysis of different parameters in simulations on thermal radiation from the jet fires has been carried out. The angular divisions' refinement for radiation model and humidity in air are shown to affect considerably the simulated radiative heat flux. 10x10 angular divisions' number was found to be the resolution, which provides independence of simulations on further refinement, for the problem under study. The presence of water vapour in air demonstrated a strong effect on the flame thermal radiation, causing variations up to 13%. Larger variations were found for different velocities at the hood for releases with higher hydrogen mass flow rate. Therefore, it is fundamental for experimental studies to make available exact measurements of test conditions to develop and validate predictive CFD models. The hydrogen inlet turbulence parameters, the absorption coefficient and turbulent Schmidt number shown to have a minor effect on radiative quantities. Turbulence intensity of 25% and turbulent length scale of $0.07 \cdot D_{eff}$ at the inlet, Hubbard and Tien's absorption coefficient model and Sc_t=0.9 were selected to describe the jet fires. Five cryogenic jet fire tests were used to validate the CFD model. For all five tests experimental radiative heat flux at 5 sensors along the jet flame was predicted within ±15% accuracy, with few exceptions. During the study, the Abel Noble EOS was found to be applicable to cryogenic releases only for low pressure (< 6 bar). Further research should be conducted to extend the domain of the CFD model applicability to high pressure cryogenic releases.

ACKNOWLEDGEMENTS

The authors are grateful to Dr. P.P. Panda for providing experimental data indispensable to conduct this numerical study. This study has received funding from EPSRC SUPERGEN H2FC Hub project (EP/J016454/1) and the Fuel Cell and Hydrogen 2 Joint Undertaking under grant agreement No.736648 (NET-Tools project) respectively. This Joint Undertaking received support from the European Union's Horizon 2020 research and innovation programme and Hydrogen Europe and N.ERGHY.

REFERENCES

[1] DOE, "Technical Assessment: Cryo-Compressed Hydrogen Storage for Vehicular Applications," 2006.

[2] A. Friedrich, W. Breitung, G. Stern, A. Veser, M. Kuznetsov, G. Fast, B. Oechsler, N. Kotchourko, T. Jordan, J. R. Travis, J. Xiao, M. Schwall, and M. Rottenecker, "Ignition and heat radiation of cryogenic hydrogen jets," *Int. J. Hydrogen Energy*, vol. 37, no. 22, pp. 17589–17598, 2012.

[3] J. E. Hall, P. Hooker, and D. Willoughby, "Ignited releases of liquid hydrogen: Safety considerations of thermal and overpressure effects," *Int. J. Hydrogen Energy*, vol. 39, no. 35,

pp. 20547–20553, 2014.
[4] P. P. Panda and E. S. Hecht, “Ignition and flame characteristics of cryogenic hydrogen releases,” *Int. J. Hydrogen Energy*, vol. 42, no. 1, pp. 775–785, 2016.
[5] A. G. Venetsanos and S. G. Giannissi, “Release and dispersion modeling of cryogenic under-expanded hydrogen jets,” *Int. J. Hydrogen Energy*, pp. 1–11, 2016.
[6] S. G. Giannissi, A. G. Venetsanos, N. Markatos, and J. G. Bartzis, “CFD modeling of hydrogen dispersion under cryogenic release conditions,” *Int. J. Hydrogen Energy*, vol. 39, no. 28, pp. 15851–15863, Sep. 2014.
[7] A. Venetsanos and J. Bartzis, “CFD modeling of large-scale LH2 spills in open environment,” *Int. J. Hydrogen Energy*, vol. 32, no. 13, pp. 2171–2177, Sep. 2007.
[8] P. P. Panda, Private communication, Sandia National Laboratories, 2016.
[9] T. H. Shih, W. W. Liou, A. Shabbir, Z. Yang, and J. Zhu, “A new eddy-viscosity model for high Reynolds number turbulent flows—model development and validation,” *Comput. Fluids*, vol. 24, no. 3, pp. 227–238, 1995.
[10] B. E. Launder and D. B. Spalding, *Lectures in Mathematical Models of Turbulence*. London, England: Academic Press, 1972.
[11] V. Yakhot and S. A. Orszag, “Renormalization Group Analysis of Turbulence,” *J. Sci. Comput.* , vol. 1, no. 1, pp. 1–51, 1986.
[12] B. Magnussen, “On the structure of turbulence and a generalized eddy dissipation concept for chemical reaction in turbulent flow,” *Am. Inst. Aeronaut. Astronaut.*, 1981.
[13] V. Molkov, V. Shentsov, S. Brennan, and D. Makarov, “Hydrogen non-premixed combustion in enclosure with one vent and sustained release: Numerical experiments,” *Int. J. Hydrogen Energy*, vol. 39, no. 20, pp. 10788–10801, 2014.
[14] J. Y. Murthy and S. R. Mathur, “A finite volume method for radiative heat transfer using unstructured meshes,” *J. Quant. Spectrosc. Radiat. Transf.*, vol. 12, no. 12, pp. 313–321, 1998.
[15] V. Molkov, *Fundamentals of Hydrogen Safety Engineering I*, 2012.
[16] NIST EOS calculator, *available from http://hydrogen.pnl.gov/tools/equation-state-calculator*.
[17] S. L. Brennan, D. V. Makarov, and V. Molkov, “LES of high pressure hydrogen jet fire,” *J. Loss Prev. Process Ind.*, vol. 22, no. 3, pp. 353–359, 2009.
[18] ANSYS Fluent, User’s Guide, 2016.
[19] C. Hubbard, G. L.; Tien, “Infrared Mean Absorption Coefficients of Luminous Flames and Smoke,” *J. Heat Transfer*, vol. 100, no. May 1978, pp. 235–239, 1978.
[20] “Emissivity of common materials,” *available from www.omega.com/literature/transactions/volume1/emissivitya.html*. .
[21] R. Schefer, B. Houf, B. Bourne, and J. Colton, “Experimental Measurements to Characterize the Thermal and Radiation Properties of an Open-flame Hydrogen Plume,” in *In Proceedings of the 15th annual hydrogen conference and hydrogen expo*, 2004.
[22] S. G. Chuech, M.-C. Lai, and G. M. Faeth, “Structure of turbulent sonic underexpanded free jets,” *AIAA J.*, vol. 27, no. 5, pp. 549–559, 1989.
[23] “Current Results weather and science facts, California average relative humidity,” *available from www.currentresults.com/Weather/California/humidity-annual.php*.
[24] L. Yan, G. Yue, and B. He, “Development of an absorption coefficient calculation method potential for combustion and gasification simulations,” *Int. J. Heat Mass Transf.*, vol. 91, pp. 1069–1077, 2015.
[25] D. Baraldi, V. Molkov, D. Makarov, J. Keenan, V. Shetsov, S. Brennan, S. Slater, S. Coldrick, O. Jedicke, K. Ren, A. Kotchourko, I. Tolias, S. Giannissi, A. Venetsanos, F. Verbecke, and A. Duclos, *The CFD Model Evaluation Protocol*, SUSANA Pro. 2016.
[26] Y. Tominaga and T. Stathopoulos, “Turbulent Schmidt numbers for CFD analysis with various types of flowfield,” *Atmos. Environ.*, vol. 41, no. 37, pp. 8091–8099, 2007.